Vortex-induced vibration in a cylinder with an azimuthal degree of freedom

D. Roberto Domínguez,[1,*] Saúl Piedra,[2,†] and Eduardo Ramos[1,‡]
[1]*Renewable Energy Institute Universidad Nacional Autónoma de México, 62580 Temixco, Mor., Mexico*
[2]*CONACYT-CIDESI, Centro Nacional de Tecnologías Aeronáuticas, 76270 Querétaro, Qro., Mexico*

(Received 4 May 2019; accepted 5 March 2021; published 1 June 2021)

We present a numerical study on the motion of a rigid cylinder promoted by its interaction with an incoming flow when the cylinder is restricted to move along the arc of a circle and thus has only one degree of freedom. The analysis also includes the description of the flow around the cylinder, which is influenced by the motion of the cylinder. The Reynolds number, based on the diameter of the cylinder and the far-away incoming flow velocity, is 180. It is considered that the diameter of the circle is three times the diameter of the cylinder and that the ratio of the cylinder to fluid densities is 1.6. The mass and momentum conservation equations in two dimensions are solved in a Cartesian grid, and the presence and motion of the cylinder are resolved using the immersed boundary method. The motion of the cylinder and the flow are two-way coupled in the sense that the aerodynamic forces that drive the displacement of the cylinder result from the fluid-solid interaction, and in turn, the flow around the cylinder is modified by its motion. We analyze the initial transient dynamics and long-time behavior for two different cases. The present results illustrate that the motion of the cylinder and the torque are quasiperiodic with cycles composed of three oscillations with different amplitudes. The stagnation point and the boundary layers are displaced periodically around the rim of the cylinder according to the incoming direction of its relative velocity with respect to the fluid. The upper and lower separation points undergo similar periodic angular displacements. This effect is superposed to the alternating vortex shedding mechanism that occurs in fixed cylinders. Two rows of alternating vortices similar to von Karman vortex street are formed downstream of the cylinder, but their centers are farther apart from the symmetry line than those generated in the wake of a fixed cylinder; this effect is closely related to the coupling between the oscillatory motion of the cylinder and the vortex shedding process. The pressure field and the instantaneous streamlines are also presented and related to the dynamical features of the cylinder motion. It is found that the pressure is the dominant effect on the dynamics of the cylinder and its magnitude and the direction of the total force on the cylinder is related to the motion of the cylinder and the genesis and emission of vortices.

DOI: 10.1103/PhysRevFluids.6.064701

I. INTRODUCTION

Vortex-induced vibrations on cylinders with freedom of motion have been the subject of intense scrutiny due to their importance in practical applications like pivoted rods and cantilevers as well as in affording a geometrically simple system to test fundamental concepts like the forces arising in fluid-structure interactions. In the present study, we aim to contribute to this field by numerically

*drdol@ier.unam.mx
†saul.piedra@cidesi.edu.mx
‡erm@ier.unam.mx

analyzing the interaction of an incoming uniform flow and a tethered cylinder that is free to move in the azimuthal direction along an arc of a circle. We focus on the description of the motion of the cylinder and the wake structure when the Reynolds number based on the diameter of the cylinder is 180, and the ratio of the diameter of the circle to the diameter of the cylinder is 3. The acceleration of gravity is not included in the analysis. This represents a real physical situation in which the acceleration of gravity is aligned with the axis of symmetry of the cylinder.

The properties of the wakes that form behind fixed cylinders are intimately related to the boundary layer around the cylinder and the forces exerted on it. Still, obviously these forces do not show in the dynamics as a fixed cylinder has effectively infinite inertia. In contrast, when the cylinder is free to move, its dynamics is complex because there is a two-way coupling between the forces generated by the flow around the cylinder and the motion of the cylinder itself that in turn perturbs the incoming flow. The number of conceivable fluid-cylinder arrangements is very large, and a general study would be practically impossible. Then, a selection of specific cases is inevitable, as can be verified from the information available in the literature. Books and reviews that have addressed specific configurations of cylinder-flow systems are, for instance, Refs. [1–4].

One of the best-documented cases is that of the vortex-induced vibrations (VIV) of elastically mounted cylinders allowed to move only in the transverse direction to the incoming flow. Experimentally, the cylinder is fixed on a frame such that springs provide restoring forces and set a natural frequency of oscillation. Informative reports on this case are Refs. [4–6]. At low mass ratio (mass of the oscillating structure/displaced mass) and low damping, three modes of vortex shedding have been reported with single or pairs of vortices shed each oscillation of the cylinder. At first sight, the case just referred to is similar to the situation we analyze in the present study. We will indeed point out some analogies in Sec. IV B 4, but there are fundamental differences. The most important one is that in the elastically mounted cylinder, there is an externally imposed natural frequency and, as it will be described in the following sections, in the present case, the restoring force is afforded by the flow itself. Out of the set of cylinders moving with externally imposed frequencies, a configuration relevant for the present study is the flow past cylinders with forced harmonic oscillations in cross flow. Several authors have looked into the problem considering specific conditions. A two-dimensional flow with $\mathrm{Re} = 500$ and a forcing frequency range between 0.75 and 1.05 times the Strouhal frequency of the fixed cylinder was studied by Blackburn and Henderson [7]. They found quasiperiodic behavior for the lift coefficient as a function of time at the lower end of the explored frequencies; for larger frequencies the lift coefficient displays weakly chaotic dynamics and fixed single frequencies. Quasi-periodic dynamics was also reported by Meneghini and Bearman [8] for $\mathrm{Re} = 200$ and forcing frequencies smaller than 0.7. It must be noted that the main difference of the configuration just commented and the case presented here, is that when the cylinder is forced, the frequencies and phases of the oscillatory motion can be arbitrarily imposed, while in the present study they are selected by the dynamics of the system.

A similar physical situation to that described in the previous paragraph and close to the one analyzed here is the flow-cylinder interaction when the rigid body is constrained to move in an arc of a circle. Devices based on pivoted cylinders VIV's have recently been proposed to extract energy from rivers and ocean currents. In these systems, the load is modeled with torsional or linear springs, which results in the inclusion of a natural oscillation frequency in the system. The amplitude of the vibration of these devices was numerically calculated by Sung *et al.* [9] who considered cylinders with circular and elliptic cross-sections and Reynolds number 500. They report that the largest amplitudes of the vibrations were obtained when the pivot is in the wake (downstream of the cylinder) and that the root-mean-square (RMS) angular velocity is an inverse function of the ratio of arm length to cylinder diameter. The experimental study on pivoted cylinders reported by Arionfard *et al.* [10] focus on the efficiency to extract energy from a constant flow with Reynolds numbers in the range from 2.9×10^3 to 2.2×10^4 where the three-dimensional effects are important [11]. The geometries used include arm lengths to cylinder diameters in the range 0.5 to 3.2, and the load is simulated with linear springs. They report that maximum efficiency conditions depend

on the springs' stiffness and the arm length, and the incoming velocity. The important effect of the added mass in a semisubmerged pivoted cylinder is described in Ref. [12].

Another configuration studied in the literature that presents similar conditions to those analyzed in the present report is the motion of cylinders in a cross-stream with a fixed lower end. Points along the pivoted cylinder axis describe ellipses of amplitude that depend on the distance to the fixed point. In most arrangements, the restoring force is provided by springs in the mount [13,14], but in other cases, the restoring force arises from the elasticity of the cylinder, and no external natural frequency is imposed [15,16]. Under some specific conditions, the pivoted cylinder describes sections of a circle, in coincidence with our case. Still, in general, its motion has two degrees of freedom, in contrast to the single degree of freedom considered in the present analysis. Thus, no direct analogy applies.

Although the fluid-pivoted cylinder has been looked into from different viewpoints due to its importance in renewable energy and other applications, it is clear that a more detailed understanding of the interplay of several effects is still far from complete. In the present report, we describe a tethered cylinder's motion to give information somewhat in detail on the angular displacement, forces, and torques under specific conditions. As described in more detail in the following sections, we chose to analyze a geometry similar to that used in the devices that extract energy from marine currents, e.g., an arm length (ratio of the diameter of the circle to the diameter of the cylinder) smaller than 3.5. We use a Reynolds number that is small for practical applications ($\mathrm{Re} = 180$), but one for which three-dimensional effects are not important. It must also be observed that given that the energy harvesting systems described in the literature incorporate an external restoring force, our study is the simplest, zero load case.

The phenomena described in the following sections are much better appreciated by examining the actual time evolution of the motion shown in the movies that can be found this article's Supplemental Material [17].

II. PHYSICAL AND GEOMETRICAL MODEL

We consider a long cylinder exposed to a uniform flow of a viscous fluid moving with a constant velocity perpendicular to the cylinder axis. We assume that the cylinder moves due to the interaction of the fluid and the rigid body, but the motion is constrained to a circle with a prescribed radius. This effectively restricts the system to move with only one (azimuthal) degree of freedom. Neglecting the end effects, the motion can be considered two-dimensional, as long as the Reynolds number based on the diameter of the cylinder is lower than about 190, where three-dimensional effects appear in its wake [11,18]. A sketch of the physical situation considered is given in Fig. 1 together with the Cartesian axis of coordinates used in the analysis.

The relevant parameters that determine the dynamics of the cylinder and the motion of the fluid are the diameter of the cylinder (d), and the diameter of the circle (D), the magnitude of the free stream velocity of the flow (U), the kinematic viscosity of the fluid (ν), and the densities of the fluid (ρ_f) and the cylinder (ρ_s). The fluid-solid interaction is made through the forces (F) that the cylinder and the fluid exert on each other and the torque (T). The analysis is more conveniently done in terms of the following nondimensional variables:

$$x^*, y^* = x/d, y/d, \quad t^* = tU/d, \quad u^*, v^* = u/U, v/U, \quad p^* = p/\rho_f U^2,$$
$$F^* = F/\rho_f U^2 d^2 \quad \text{and} \quad T^* = T/\rho_f U^2 d^3, \tag{1}$$

where u and v are the velocity components in the x and y directions, respectively. Three nondimensional parameters can be defined, namely, the Reynolds number ($\mathrm{Re} = Ud/\nu$), the ratio of the diameter of the cylinder to the diameter of the circle (d/D), and the density ratio ($m^* = \rho_s/\rho_f$).

Most of the dynamical analysis of the cylinder and surrounding flow in the following sections will be made in terms of the streamwise and transverse forces, F_x and F_y, respectively. Still, in

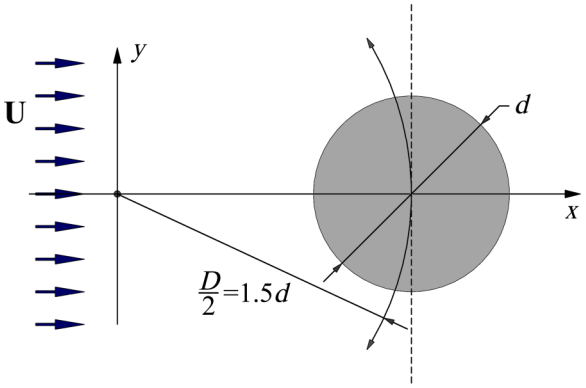

FIG. 1. Sketch of the physical situation analyzed. The cylinder diameter is d, and the diameter of the circle where the cylinder moves is $D = 3\,d$. The incoming flow moves from left to right, and upstream of the cylinder, the fluid has a uniform velocity $\mathbf{U}$.

aerodynamics, the forces on a body are conveniently decomposed in drag and lift depending on whether they are parallel or perpendicular to the relative motion of the body and the fluid. For the sake of completeness, we give the expressions for drag and lift. Figure 2(a) shows the incoming flow velocity ($\mathbf{U}$) and the tangential velocity of the cylinder ($\dot{\theta}D/2$) at a position of the cylinder when θ and $\dot{\theta}$ are positive. The vector sum of the two velocities is denoted by $\hat{\mathbf{u}}$ and indicates the instantaneous direction of the incoming flow as described from a frame of reference attached to the cylinder. The angle θ^* is defined by

$$\theta^* = \arccos \frac{\hat{\mathbf{u}} \cdot \mathbf{U}}{|\hat{\mathbf{u}}||\mathbf{U}|}. \tag{2}$$

The direction of the force that results from the flow-cylinder interaction $\hat{\mathbf{F}}$ varies as a function of the position of the cylinder, as will be discussed at length in the following sections, but it is only the projection of the resultant force on the tangential direction that produces torque. The component of the force in the radial direction has no effect on the dynamics because it is assumed that the cylinder is at a fixed distance from the center. The tangential force can be projected in the *local* streamwise and transverse directions, i.e., along the direction of the resultant velocity $\hat{\mathbf{u}}$ which we call $\mathbf{F_D}$ and along the direction perpendicular to it, $\mathbf{F_L}$. This identifies the drag and lift forces. From

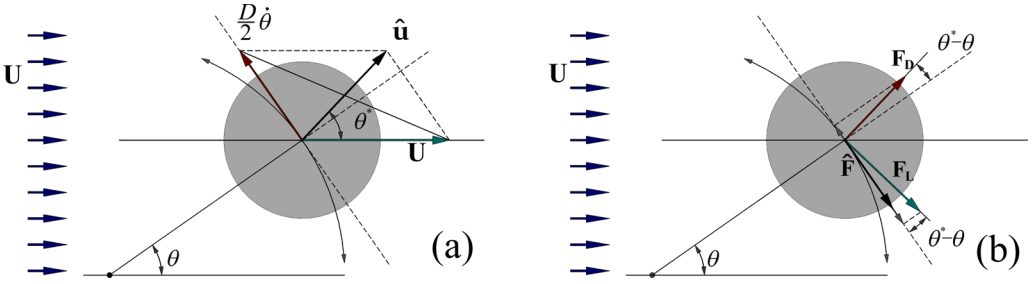

FIG. 2. (a) Definition of the relative velocity of the cylinder ($\hat{\mathbf{u}}$) for a given azimuthal position (θ) and angular velocity ($\dot{\theta}$) and the angle between the relative velocity and the direction of the incoming flow (θ^*). (b) Definition of the tangential force ($\hat{\mathbf{F}}$) and the drag and lift forces, $\mathbf{F_D}$ and $\mathbf{F_L}$, respectively.

the geometry of the system explained in Fig. 2, it can be observed that the following equality holds:

$$-\rho\pi\frac{1}{9}\left(\frac{D}{2}\right)^3\ddot{\theta} = \mathrm{F_L}\cos(\theta^* - \theta) - \mathrm{F_D}\sin(\theta^* - \theta), \tag{3}$$

where the forces in the previous equation are defined per unit length of the cylinder.

The lift and drag forces in terms of the streamwise (F_x) and transverse (F_y) forces, as defined by the incoming flow $\mathbf{U}$ are

$$\mathrm{F_L} = \frac{\mathrm{F}_y\cos\theta^* - \mathrm{F}_x\sin\theta^*}{\cos(2\theta^* - \theta)} \quad \text{and} \quad \mathrm{F_D} = \frac{-\mathrm{F}_y\sin(\theta^* - \theta) + \mathrm{F}_x\cos(\theta^* - \theta)}{\cos(2\theta^* - \theta)}. \tag{4}$$

III. MATHEMATICAL MODEL AND NUMERICAL IMPLEMENTATION

The mathematical model is based on the immersed boundary method presented in Ref. [19], see also Ref. [20]. Considering a fluid in which one or more solids can be immersed, when a regular grid is used to discretize the domain, some control volumes will be in the fluid or solid regions, and others, partially in the fluid and partially in the solid. To identify cells inside and outside the solid, we define an indicator field using the Heaviside step function as follows:

$$I(\mathbf{x}) = \begin{cases} 1 & \text{inside the fluid,} \\ 0 & \text{inside the solid.} \end{cases} \tag{5}$$

The indicator field is constructed based on the fact that the solid-fluid interface marks the jump on the indicator function and this jump becomes in a sharp gradient on the Cartesian grid. The gradient of the indicator field in a discrete form can be expressed as

$$\nabla I_{ij} = \sum_l \Delta I \omega_{ij}^l \mathbf{n}_l \frac{\Delta L_l}{h^2}, \tag{6}$$

where $\mathbf{n}_l$ and ΔL_l are, respectively, the normal vector and the length of element l, and h is the spatial discretization interval in the regular grid. The symbol ω_{ij}^l is the discrete form of the Dirac delta function and is the weight of grid point ij for the element l of the interface. In the present study, the weighting function developed by Peskin [21] has been used to compute the gradient of the indicator field. Once the grid gradient of the indicator field has been constructed, the field can be recovered by taking the numerical divergence of the grid indicator field gradient. In symbols,

$$\nabla^2 I = \nabla \cdot \nabla I_{ij}. \tag{7}$$

The left-hand side of Eq. (7) is approximated by standard central differences, and solving the resulting Poisson equation with the appropriate boundary conditions yields the indicator field everywhere. After the indicator field has been calculated, it is possible to find the velocity in any cell of the computational domain with the expression

$$\mathbf{u}^*(\mathbf{x}) = I(\mathbf{x})\mathbf{u}_f^*(\mathbf{x}) + [1 - I(\mathbf{x})]\mathbf{u}_s^*(\mathbf{x}), \tag{8}$$

where $\mathbf{u}_f^*$ is the velocity in the fluid region, and $\mathbf{u}_s^*$ is the velocity of the solid. From the mathematical perspective, since the indicator field is represented as a Heaviside function, a no-slip boundary condition at the solid surface is imposed. However, the numerical implementation of the discrete form of the step function creates a transition zone where the indicator function takes values from zero inside the solid to one outside of it. Then, in a strict sense, the no-slip boundary condition at the interface depends on the shape and thickness of such transition zone. This is a well-known behavior of the immersed boundary and fictitious domain methods, and many approximations have been developed to improve the accuracy of the solutions, in this work, the strategy presented in Ref. [19] was used to reduce the effect of the transition zone.

The velocity in the fluid is dictated by the mass and momentum conservation equations for incompressible flows:

$$\nabla \cdot \mathbf{u}_f^* = 0, \tag{9}$$

$$\frac{\partial \mathbf{u}_f^*}{\partial t^*} + \nabla \cdot \mathbf{u}_f^* \mathbf{u}_f^* = -\nabla p^* + \frac{1}{\mathrm{Re}} \nabla^2 \mathbf{u}_f^*, \tag{10}$$

where p^* is pressure. The motion of the cylinder is modeled by the Euler equations [22]. In general, for an arbitrary motion of a solid body immersed in a fluid, both Newton and Euler equations must be solved to calculate the velocity of the solid body but, in the two-dimensional case described in Fig. 1, those equations are simplified by using the constraint that the motion is limited to a circle. Then, the translational velocity of the cylinder ($\mathbf{u}_{sc}^*$) can be found as [23]

$$\mathbf{u}_{sc}^* = \frac{D}{2} \dot{\theta} (\cos\theta, \sin\theta). \tag{11}$$

With this simplification, only one differential equation for the angular velocity is required to calculate the total velocity of the cylinder as follows:

$$(m^* + m_a^*) \frac{d\dot{\theta}}{dt} = T^*, \tag{12}$$

where m_a^* is the added mass of the cylinder. Observe that in this case, the added mass in terms of the scaled variables is $m_a^* = 1$. In this two-dimensional case, the torque is a pseudo-vector with only one component in the direction perpendicular to the motion plane. Once the velocities of the centroid are known, the velocity field inside the body is computed by

$$\mathbf{u}_s^* = \mathbf{u}_{sc}^* + \mathbf{r}^* \times \dot{\theta} \hat{\mathbf{k}}, \tag{13}$$

where the $\mathbf{r}^*$ is a position vector, i.e., the distance to any point inside the solid from the center of rotation of the cylinder, and $\hat{\mathbf{k}}$ is a unit vector perpendicular to the motion plane. The coupling between the equations in the fluid and the solid regions is the hydrodynamic force ($\mathbf{F}^*$) and torque (T^*) acting over the solid. The hydrodynamic force and torque are found integrating the stress tensor over the rigid body-fluid boundary S [24]:

$$\mathbf{F}^* = \int_S \left\{ -p^* \mathbf{I} + \frac{1}{\mathrm{Re}} [\nabla \mathbf{u}_f^* + (\nabla \mathbf{u}_f^*)^\intercal] \right\} \cdot \hat{\mathbf{n}} dS, \tag{14}$$

and

$$T^* = \int_S \mathbf{r}^* \times \left\{ -p^* \mathbf{I} + \frac{1}{\mathrm{Re}} [\nabla \mathbf{u}_f^* + (\nabla \mathbf{u}_f^*)^\intercal] \right\} \cdot \hat{\mathbf{n}} dS, \tag{15}$$

where $\mathbf{I}$ is the identity tensor and $\hat{\mathbf{n}}$ is the unit vector perpendicular to S. The symbol $(\cdot)^\intercal$ indicates the transpose of the tensor. As it is usually done, the two-dimensional model can be understood as a three-dimensional model with the force and the torque interpreted as per unit length in the direction normal to the motion plane.

The computational domain consists of a rectangle with free slip boundary conditions at the upper and bottom walls, inlet flow on the left, and outflow on the right wall. The size of the computational domain is 24×12 cylinder diameters, and it was discretized with a regular grid of 768×384 control volumes in the x and y directions, respectively. The fixed time step $\Delta t^* = 0.0002$ for all simulations. A study on the mesh fineness, domain size, and time step is presented in the Appendix.

The model described in the previous section was implemented according to the following steps. First, Navier-Stokes equations are solved using the standard finite-volume method and, the solid body is treated as a fictitious fluid with high viscosity. The hydrodynamic force and torque are integrated through Eqs. (14) and (15) and used in the Euler equation to compute the translational and angular velocity of the solid body. Once the centroid velocity of the solid body is computed,

the velocity of any point in the solid region is calculated by Eq. (13). Finally, the whole domain's velocity is corrected using Eq. (8).

Two initial conditions have been considered in the analysis. We chose these conditions because they are relevant in the context of real, experimental observations.

Case I:

$$\mathbf{u}^* = \mathbf{0}, \quad \mathbf{u}^*_{cs} = \mathbf{0}, \quad \text{and} \quad \theta = \dot{\theta} = 0. \tag{16}$$

The cylinder is free to move as the flow starts developing. Note that in contrast to the velocities, there is no time derivative for θ in the equations. However, an initial condition for the indicator function I [Eq. (5)] must be provided to specify the position of the cylinder at the onset of the simulation. Also, the following technical comment is in order: When running the simulation program, it was found that the cylinder position should be fixed for the initial time steps (<10 t*) to prevent the run from crashing due to the large initial gradients. This, however, does not have a noticeable impact on the dynamics of the system because of the small size of the time interval and the minimal velocities acquired by the cylinder in this time interval.

Case II:

$$\mathbf{u}^* = \mathbf{u}^*_{vK}, \quad \mathbf{u}^*_{cs} = \mathbf{0}, \quad \text{and} \quad \theta = \dot{\theta} = 0. \tag{17}$$

In this case, the cylinder position is fixed, and its velocity is zero. The initial flow velocity $\mathbf{u}^*_{vK}$ is the velocity field that corresponds to the flow around and the wake of a fixed cylinder (von Karman vortex street). In the simulation, this condition is implemented in the following way. Initially, the cylinder is constrained to remain at its initial position long enough for the wake to develop. Then, the restriction is removed at $t^* = t^*_r$, and the cylinder is free to move according to the interaction forces.

IV. RESULTS

In the present study, we keep the ratio $D/d = 3$ and consider that the Reynolds number based on the cylinder's diameter is 180. The density ratio, $m^* = 1.6$.

Before presenting the dynamics of the system under analysis, it is useful to briefly comment on the time-dependent evolution of the wake of a fixed cylinder. At Re = 180, vortices are formed as the flow starts flowing around the cylinder, and an alternating force in the transversal direction is exerted on the cylinder. Initially, this oscillatory force grows linearly with time. Still, at a certain stage ($\sim$50 t^*), the transversal force on the fixed cylinder grows very fast for a short period ($\sim$ 25 t^*) before reducing its amplitude to attain the constant amplitude characteristic of the fully developed von Karman vortex street.

A. Dynamics of the cylinder

1. Azimuthal position and velocity

Figure 3 shows the position of the center of the cylinder as a function of time for initial conditions corresponding to Cases I and II. The last columns display in more detail the initial and long-term behavior.

In the first example, shown in Fig. 3(a) (upper row), the cylinder is free to move in the azimuthal position as dictated by the forces generated by the flow around it; this corresponds to the initial conditions of Case I [Eq. (16)]. At early times $t^* < 50$, the cylinder remains practically motionless and then oscillates with a small amplitude around the position $\theta = 0$. Subsequently, the cylinder keeps oscillating with high frequency, but its average position displays few large excursions to eventually settle around the approximate position $\theta = 0$ after 600 time units. In the long-time dynamics, the cylinder oscillates with an approximate maximum amplitude of 0.48 radians ($\pm$ 28.3°) and with a dominant frequency of 0.13 1/t* (see upper panel of Fig. 4). The motion is not strictly periodic, but we can identify an approximate repeating cycle composed of three oscillations. See the time interval

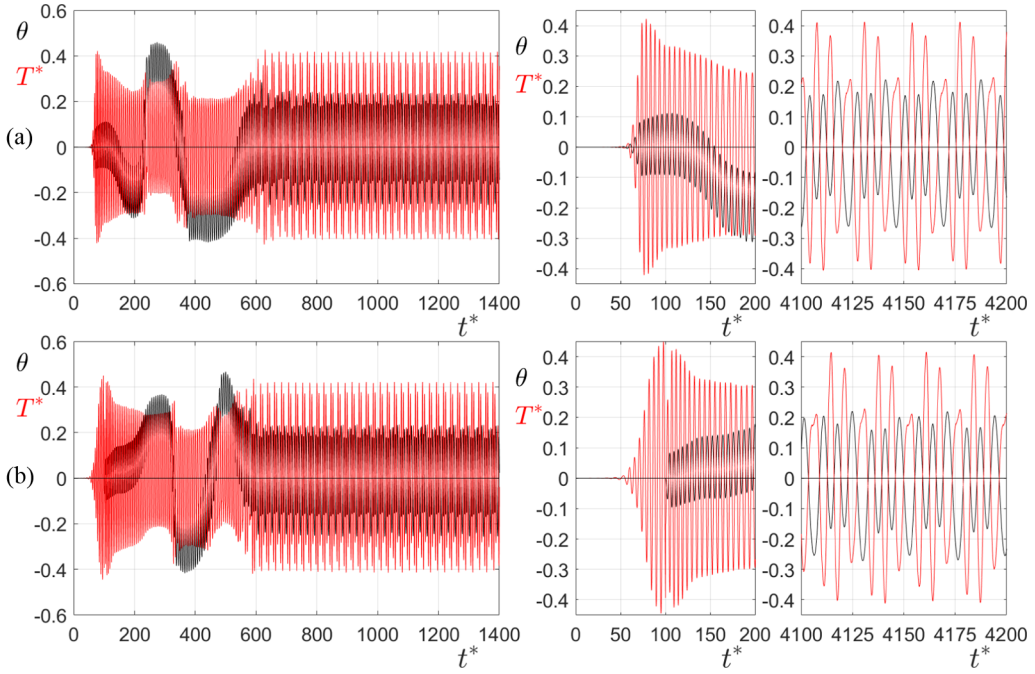

FIG. 3. Position of the center of the cylinder (θ, black trace) and nondimensional torque (T^*, red trace) as functions of nondimensional time (t^*) for different initial conditions. (a) Case I; (b) Case II, $t_r^* = 100\,t^*$. The two last columns contain amplifications of the initial and long-term behavior, respectively.

$4130 < t^* < 4150$ of the plot on the right upper row of Fig. 3. This oscillation will be described in greater detail below. The traces in Fig. 3 indicate that the azimuthal position and the torque are always out of phase. Observe that a positive (negative) torque promotes a counterclockwise (clockwise) motion.

In Case II, shown in Fig. 3(b), the cylinder is fixed for 100 time units ($t_r^* = 100\,t^*$), long enough for the von Karman vortex street to develop around a fixed cylinder, then, the constraint is relaxed, and the cylinder is free to move along the azimuthal coordinate. The cylinder oscillates as in the first case, and its time average position wanders around $\theta = 0$. Eventually, after a transient of approximately the same duration as the first case, the cylinder motion settles in a complex oscillation with high frequency and an average azimuthal position θ close to zero. The long-term behavior is found to be similar but not identical in the two cases analyzed. Inspection of the last column of

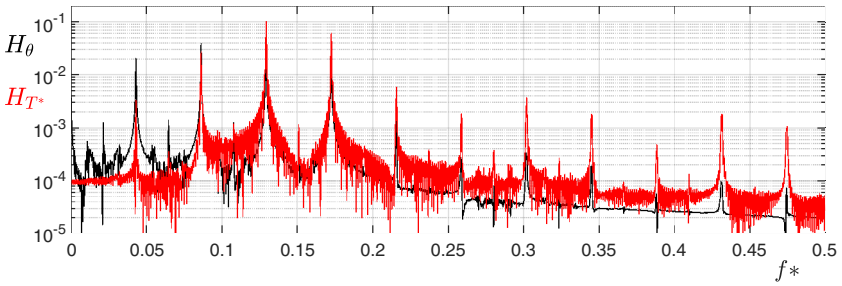

FIG. 4. Fourier spectrum of the angular position, H_θ, black line; torque, H_{T^*}, red line. The initial conditions used correspond to Case I.

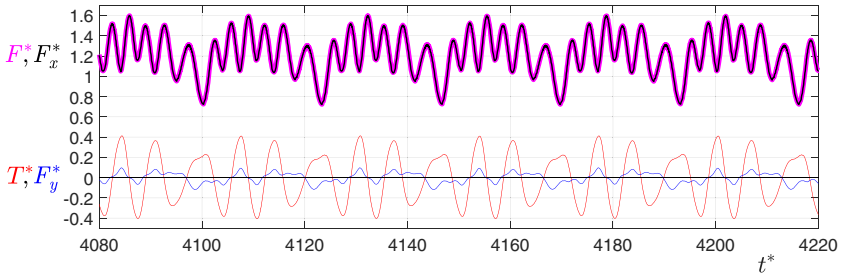

FIG. 5. Total (F^*), streamwise (F_x^*), and transverse (F_y^*) forces and torque (T^*) on the cylinder as functions of time.

Fig. 3 (see also the upper panel of Fig. 9), the swings with larger amplitude in the azimuthal position correspond to smaller torques and vice-versa.

The Fourier spectrum of the angular position for Case I is shown in Fig. 4. We considered only $t^* > 800$ to disregard the initial transient influence in calculating the Fourier transform. The Fourier analysis was made for Case II with two restraint times ($t_r^* = 50$, 100), and it was found that in all runs, the frequency $f_{\theta 3}^* = 0.13\,1/t^*$ is dominant with major components with frequencies $f_{\theta 1}^* = f_{\theta 3}^*/3$, $f_{\theta 2}^* = 2f_{\theta 3}^*/3$, and $f_{\theta 4}^* = 4f_{\theta 3}^*/3$.

The time evolution of the velocity of the cylinder is directly calculated from its position, and as expected, it is found that its extreme values ($|\dot{\theta}_M|$) and zeros are located at $\theta = 0$ and at the extreme values of the azimuthal displacement, respectively. The maximum ratio of the induced velocity to the incoming flow velocity is $\sim D|\dot{\theta}_M|/2U \sim 0.25$, and the resultant direction of the incoming flow as defined from the axis of coordinates fixed on the cylinder is $|\theta^*| < 0.25$ (14°), see Fig. 2.

2. *Force and torque*

The force and torque on the cylinder can be calculated using Eqs. (14) and (15), respectively. Figure 3 shows the magnitude of the nondimensional torque as a function of time for the two initial conditions considered. As previously noted, the torque and angular position are always out of phase, indicating that the two signals' dominant frequencies are the same. This is corroborated in Fig. 4 where the torque for Case I frequency spectrum is presented. The Fourier spectrum shows that the dominant frequency of the torque oscillation is equal to that of the angular displacement, i.e., $f_{T^*}^* = 0.13\,1/t^*$ with major components $2f_{T^*}^*/3$, $4f_{T^*}^*/3$, and $5f_{T^*}^*/3$. It is important to remark that the torque spectrum is richer than that of the position for high frequencies. This last feature is consistent with the presence of a complex maximum that appears every three swings as it is more clearly observed at $t^* = 4100$, 4123, … in Fig. 5. Although sharing dominant frequencies with the azimuthal position, the torque has Fourier modes with smaller amplitude in the low frequencies and larger amplitude in the high frequencies range. In Fig. 3 it is also observed that the torque oscillates approximately around zero for all times, with the swings less symmetric during the transient. As expected, the torque oscillation amplitude is larger when the cylinder is fixed and reduces when the cylinder is released at $t^* = 100$, as it is illustrated in the central panel of Fig. 3(b). It is also found the cylinder oscillations with larger amplitude correspond to torque oscillations with smaller amplitude.

To describe the force on the cylinder, it is convenient to use its projections in the streamwise (F_x^*) and transverse (F_y^*) directions and its magnitude ($F^* = \sqrt{F_x^{*2} + F_y^{*2}}$). Figure 5 shows these variables and the torque on the cylinder as functions of time for Case I. The total and streamwise forces are practically indistinguishable and are always positive. The Fourier analysis of this signal indicates that the dominant modes have frequencies $f_{F^*}^* = 0.043\,1/t^*$ ($= f_{\theta 1}^*$) and the cluster $2f_{F^*}^*$, $3f_{F^*}^*$, $4f_{F^*}^*$, $5f_{F^*}^*$, and $7f_{F^*}^*$ which have comparable amplitudes. The transverse force is much smaller, oscillates around zero, and has a richer content of high-frequency Fourier components.

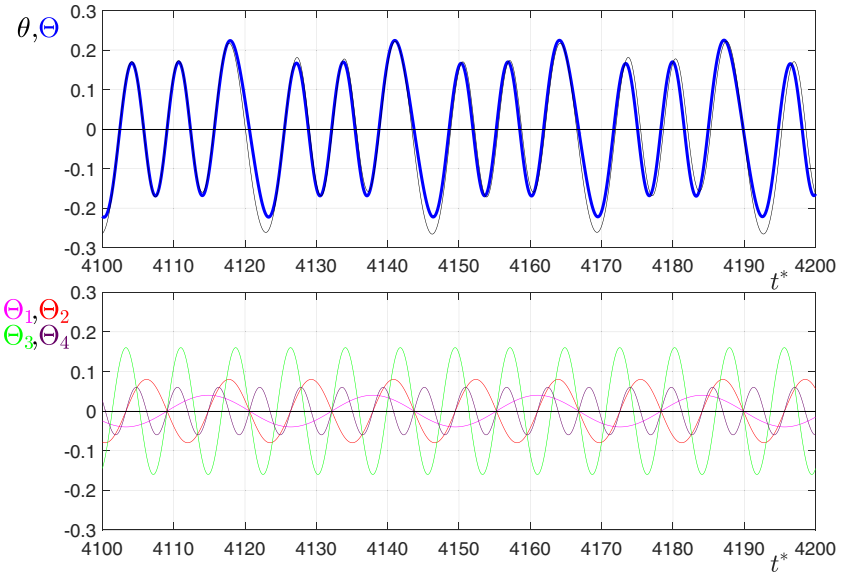

FIG. 6. Vibration analysis. Upper panel, azimuthal position of the cylinder θ (thin gray line) and its periodic reconstruction Θ (thick blue line), Eq. (18). Lower panel, individual waves in Eq. (18).

3. Vibration analysis

The long-term azimuthal position of the cylinder displayed in the upper right column of Fig. 3 (Case I) is a quasiperiodic signal with a cycle composed of three oscillations, one of them with a slightly larger amplitude than the other two. The cycle spans approximately 23 nondimensional time units. The signal can be closely represented with four Fourier components with frequencies that correspond to the dominating frequencies displayed in Fig. 4.

Figure 6 shows the relative influence of each of the four dominant frequencies in the Fourier spectra of Fig. 4(a). The upper panel shows the actual position of the cylinder (black line) and the reconstructed periodic function defined by

$$\Theta = \sum_{n=1}^{4} \Theta_n, \tag{18}$$

where

$$\Theta_1 = 0.04\sin(2\pi f^*_{\theta 1} t^*), \quad \Theta_2 = -0.08\sin(2\pi f^*_{\theta 2} t^*),$$
$$\Theta_3 = 0.16\sin(2\pi f^*_{\theta 3} t^*), \quad \Theta_4 = 0.06\sin(2\pi f^*_{\theta 4} t^*).$$

The frequencies $f^*_{\theta 1} = 0.043$, $f^*_{\theta 2} = 0.087$, $f^*_{\theta 3} = 0.13$, $f^*_{\theta 4} = 0.173$, are the dominant Fourier components of the azimuthal position. Although the higher frequencies are integral factors of the smallest, the most energetic frequency corresponds to $f^*_{\theta 3}$. As described in more detail below, the frequency with the largest coefficient corresponds to the vortices' emission. It is also interesting to observe that all components have zero relative phase except for the component with frequency $2f^*_{\theta 3}/3$ whose relative phase is π. The lower panel of Fig. 6 displays the individual waves of Eq. (18).

It must be noticed that the periodical reconstruction under predicts the largest negative oscillation amplitude of θ and also that it lags behind; this last effect is barely noticeable in the last swing of θ in the upper panel of Fig. 6. The differences are due to the Fourier components present in the original signal and absent in the reconstruction.

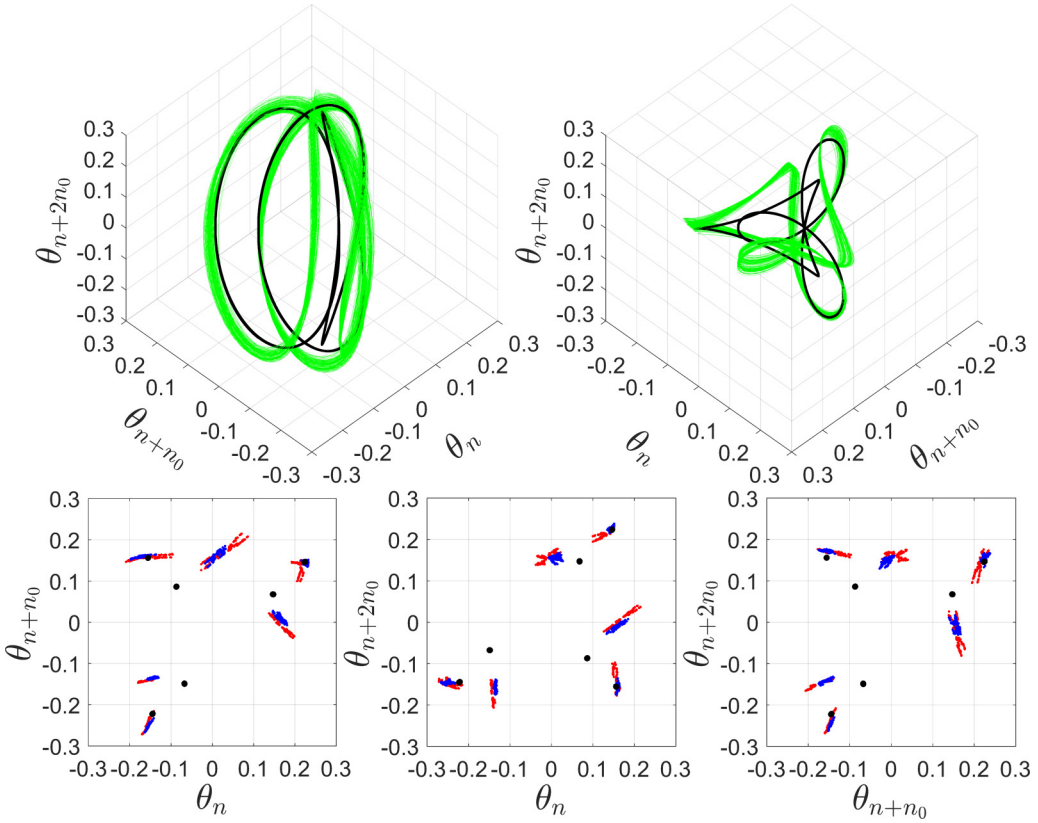

FIG. 7. Upper figures: Three-dimensional attractor in space $\theta_n, \theta_{n+n_0}, \theta_{n+2n_0}$ with delay time $n_o = 1/f^*_{\theta 3}$ for Case I. Lower figures: Poincare maps for Cases I and II. The black thick lines in the upper figures and the black dots in the lower figures represent the simplified expression given in Eq. (18).

It was previously commented that the cylinder's azimuthal position as a function of time is quasiperiodic, i.e., it is a time series that is apparently periodic but does not exactly repeat itself. To illustrate the small differences found, we plot the attractor in a 3D embedding phase space using the inverse of the dominant frequency $n_o = 1/f^*_{\theta 3}$ as the delay interval. The upper row of Fig. 7 shows the attractor from two viewpoints to better appreciate its structure. The three oscillations that compose a cycle are clearly displayed. In the lower row of the same figure, we show the Poincaré maps of the attractor obtained for a horizontal and two mutually perpendicular vertical planes that contain the point (0,0,0). The structure of the attractor is filiform with branches bifurcating from a common point, as can be seen from the blue and red clusters of points in the lower panels of Fig. 7 that correspond to Cases I and II in Figs. 3(a) and 3(b), respectively. As can be appreciated, the structure of the attractor is the same for the two cases.

The closed black line is Θ, the simplified representation of the cylinder's azimuthal position. The black dots in the lower row constitute the Poincaré map of Θ and are isolated points as it corresponds to a closed loop in phase space.

B. Flow around and downstream the cylinder

1. Velocity at downstream point

A complementary analysis of the evolution of the cylinder position can be made in terms of the downstream velocity. The upper panel of Fig. 8 shows the streamwise u^* and transverse v^* velocity

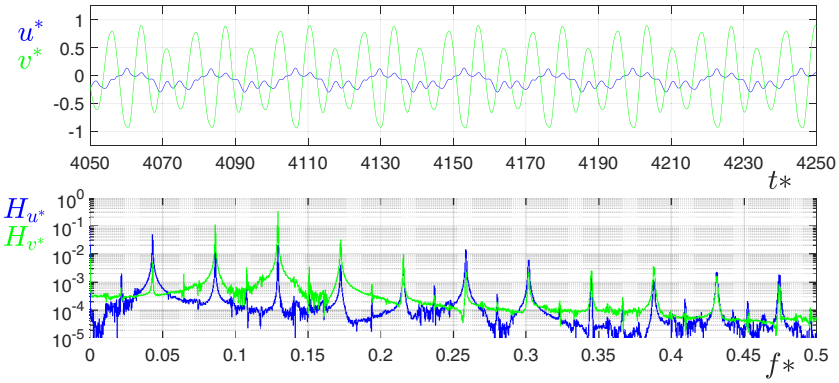

FIG. 8. Upper panel: Velocity components u^* and v^* of the fluid for Case I at a position 4.5 diameters downstream from the center of the cylinder and $\theta = 0$ as functions of time. Lower panel: Fourier spectra of u^* and v^* signals.

components as functions of time at a point four and a half diameters downstream of the center of the cylinder at position $\theta = 0$. Data in Secs. IV B and IV C correspond to Case I for long times after the transient has died out. The oscillation of the transverse velocity is symmetric with respect to $\theta = 0$ and is composed of cycles of three increasingly amplitude swings. In contrast, the streamwise velocity's oscillation is not symmetric with respect to zero, displaying dominant-negative values. The amplitude of the v^* oscillation is smaller and more complex than the transverse counterpart. We found that the velocity traces for Case II described in Fig. 3 display the same behavior and are not shown.

The Fourier spectra of u^* and v^* are plotted in the lower panel of Fig. 8. Both signals dominant modes are the same, but the frequency of the highest peak of u^* is one-third of its counterpart of v^*. Also, note that the highest peak of v^* is present in the spectrum of u^* albeit with smaller energy content. Observe that all frequencies are multiples of the cylinder's azimuthal position lowest frequency ($f^*_{\theta 1} = 0.043$).

As can be observed from the lower panel of Fig. 8, the dominant frequencies of u^* and v^* are

$$f^*_{u^*} = \frac{f_u d}{U} = 0.0435 \quad \text{and} \quad f^*_{v^*} = \frac{f_v d}{U} = \mathrm{St}_{v^*} = 0.13.$$

In the last expression, we emphasize that the transverse velocity frequency is usually identified with the Strouhal number St_{v^*}. The ratio of the Strouhal oscillation frequency (St_{v^*}) to the fixed cylinder Strouhal frequency[1] is $0.13/0.19 = 0.68$. It is interesting to observe that the occurrence of quasiperiodic motion for this range of frequencies is consistent with the results obtained for forced cross flow oscillating cylinders for $\mathrm{Re} = 200$ [8] and 500 [7] who report quasiperiodic or beating dynamics for forcing frequencies smaller than 0.77 times the Strouhal number of the fixed cylinder.

2. Vorticity field

A general picture of the vorticity field around the cylinder and vortex shedding in one cycle of the cylinder's oscillation for Case I and times $t^* > 600$ is shown in Fig. 9. The vorticity distribution near the cylinder is more complex than that of a fixed cylinder, and the array of vortices in the wake are less regular than those in a fixed cylinder. More detailed descriptions of the vorticity distribution features around the cylinder and in the wake are given in Secs. IV B 3 and IV B 4, respectively.

[1]The nondimensional frequency of the transverse velocity of a fixed cylinder, for $\mathrm{Re} = 180$ is $\mathrm{St} \approx 0.19$ [25].

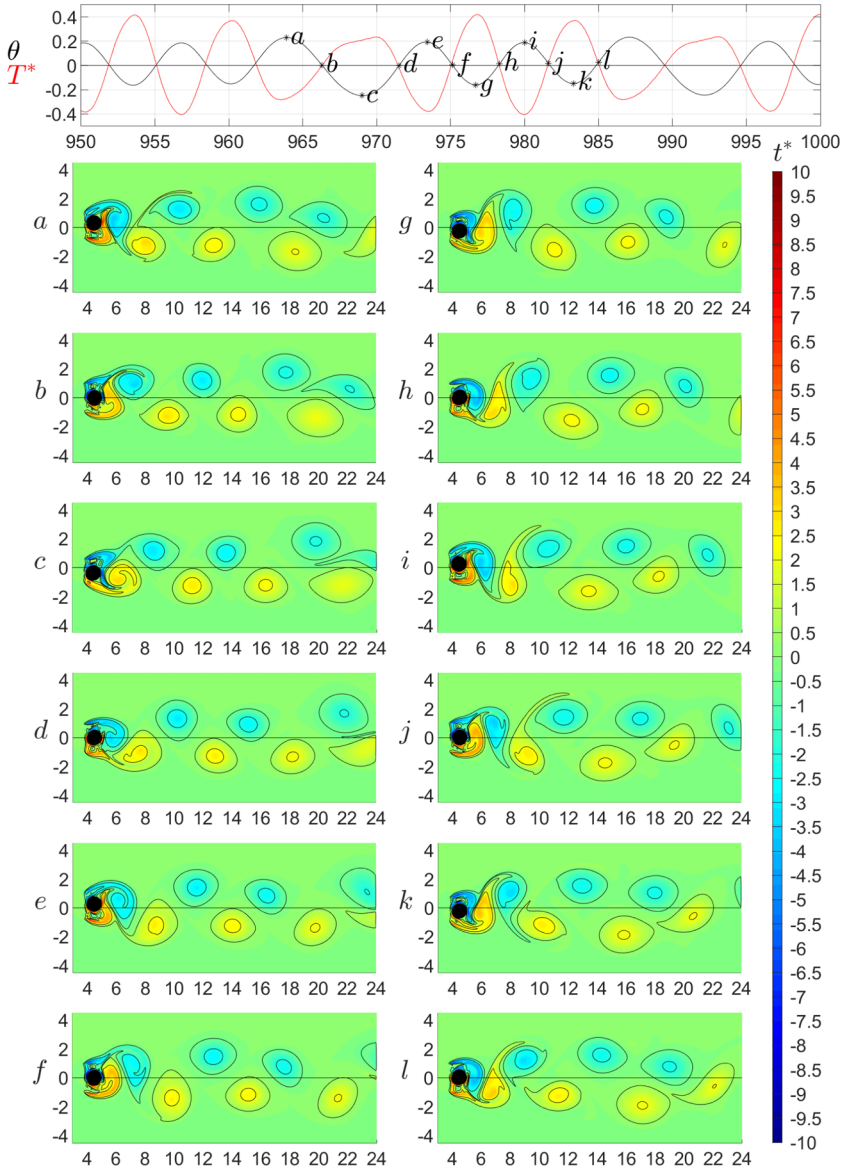

FIG. 9. Upper panel, angular position, and torque as functions of time. Lower panel, snapshots of vorticity field. The times at which the vorticity fields were obtained are indicated in the upper panel.

The angular position and the cylinder's torque as functions of time are given in the upper panel of the figure. The black dots indicate the time when the snapshots of the vorticity field are illustrated. As explained previously, the cycle is composed of one large swing followed by two smaller amplitude oscillations.

To simplify the near wake dynamics description, it is useful to recall the spatial distribution of the dynamic structures leading to vortex shedding from a fixed cylinder shown in Fig. 10. The geometrical and physical properties of the vorticity in the near wake of a fixed cylinder are explained in detail in Ref. [7] for a specific Reynolds number. Here we focus only on the features that will help describe the near wake of a tethered cylinder.

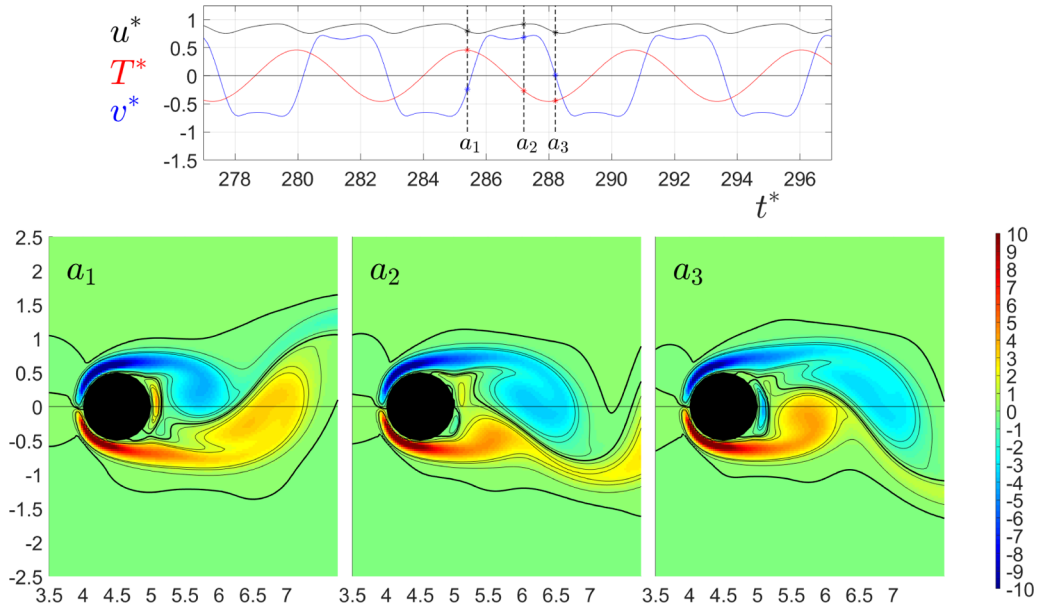

FIG. 10. Vorticity field in the surrounding area of the fixed cylinder. Upper panel: velocity components and torque as functions of time. Lower panel: vorticity fields at times indicated in the upper panel.

The wake of a fixed cylinder in cross flow starts with the production of vorticity at the surface of the cylinder in response to wall-tangential components of pressure gradient. Vorticity diffuses away from the cylinder and concentrates in the two shear layers above and below the stagnation point. These regions with high vorticity of opposite signs grow fed by circulation from their shear layers as they move backward along the cylinder's surface. At the separation point, further supply of circulation is cut off by the entrainment of counter-rotating vorticity supplied by a short-lived, small pocket of vorticity formed near the cylinder's rear side. The main flow past the cylinder then sweeps the vorticity, and for Reynolds numbers 180, the vorticity tongues are strong enough in the near wake to draw the opposite shear layer across the symmetry line. As a consequence, vortices are shed and convected downstream. The flow's characteristic spatial magnitude is the cylinder's diameter, and the vortical structures in the wake display this scale.

3. Near wake

The mechanism of vortex formation and shedding is similar to that occurring in the fixed cylinder case, namely, the generation of vorticity in the boundary layer at the surface of the cylinder and its detachment due to adverse pressure gradient, but, in the present case, the azimuthal displacement modifies the relative motion between the cylinder and the incoming flow. The detail of the vorticity field near the cylinder is shown in Fig. 11. As described previously, the stagnation point in the cylinder moving with one azimuthal degree of freedom is not always at the same spot but moves along the rim of the cylinder, with the largest displacement occurring when the cylinder is at position $\theta = 0$ and has the largest azimuthal velocity. Near the cylinder's surface, the formation of the high-vorticity region near the stagnation point is symmetric and similar to that of the fixed cylinder. However, the separation region and the structure of the high vorticity region farther away from the cylinder is distinctly different from that of the fixed cylinder. The high vorticity regions have complex structures that pulsate, expanding and contracting synchronously with the cylinder oscillation motion. In its largest extension, the region comprises two tongue-like structures with

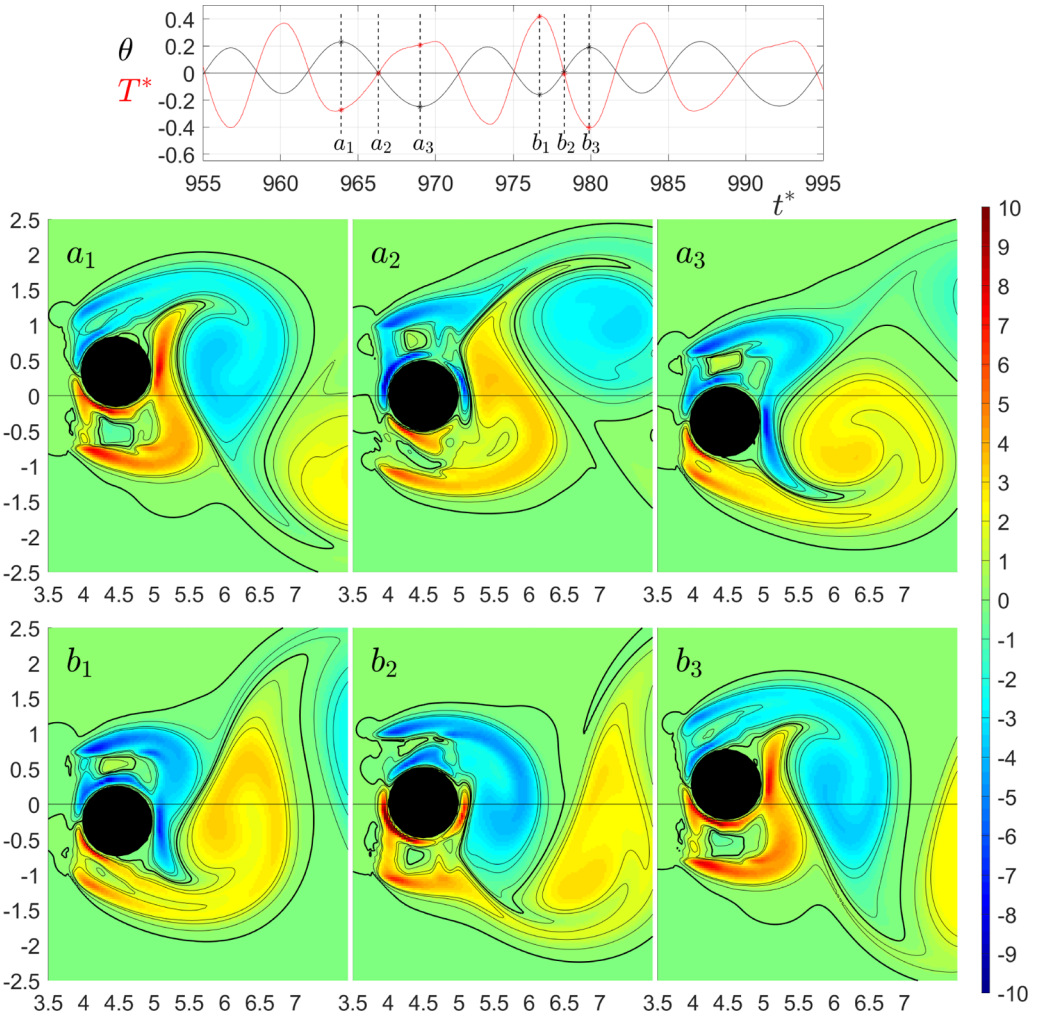

FIG. 11. Vorticity field in the surrounding area of the cylinder for $955 < t^* < 995$. For reference, see Figs. 3(a) and 9.

high vorticity separated by a zone with no vorticity or low-intensity vorticity of opposite sign. In its smallest extension, the two tongues merge, and the low vorticity zone practically disappears. Remarkably, the structure described is not swept away by the external flow but remains approximately at the same position during the whole cycle. Another major feature of the vorticity distribution is that the intense vorticity zone is far larger than in the fixed cylinder. This is an obvious consequence of the cylinder's azimuthal motion, where a characteristic magnitude is not the diameter of the cylinder but the diameter plus its displacement. In the particular case under analysis, this magnitude amounts to approximately $2d$. Although the picture varies slightly for each of the three oscillations that compose one cycle (see Fig. 11), the vorticity distributions are similar. A pocket of intense vorticity is formed near the stagnation point at the lee side of the cylinder in a similar fashion to the fixed cylinder, but its intensity and extension are larger due to the azimuthal motion of the cylinder. Specifically, the pocket merges with the (oversized) vorticity tongues when the cylinder is at its extreme positions, and this combination produces an efficient cutoff mechanism for vortex shedding.

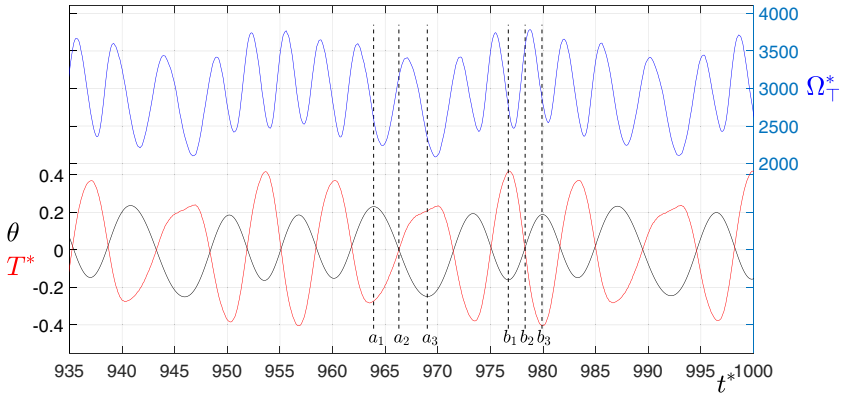

FIG. 12. Accumulated vorticity (Ω^*_T) as defined in Eq. (19) in a $0.1d$ width ring around the cylinder as a function of time. The azimuthal position of the cylinder and the torque are also shown for reference.

The swing with the maximum torque difference occurring between b_3 and b_1 in Fig. 11, coincides with the smallest azimuthal displacement. This swing also has the shortest time interval. Correspondingly, the swing with the smallest torque difference (a_3-a_1) coincides with the largest azimuthal displacement difference and has the longest time interval.

The dynamics of the cylinder and the vorticity generated in its vicinity can be linked as follows. As described previously, the cylinder motion cycle is composed of three oscillations or swings in the azimuthal position. The total vorticity accumulation (Ω^*_T) in the immediate vicinity of the cylinder can be evaluated by integrating the vorticity field in a ring around the cylinder, i.e.,

$$\Omega^*_\mathsf{T} = \frac{\int_A |\nabla \times \mathbf{u}_f| dA}{A}, \tag{19}$$

where A is the area of a small ring around the cylinder.[2]

In Fig. 12, it can be observed that Ω^*_T is an oscillatory function of time with a fast frequency equal to $2f^*_{\theta 3}$ indicating that two vortices are generated in each swing of the cylinder. Also, from the figure, it can be appreciated that local maximums of Ω^*_T happen at the start of deceleration, near zero-velocity points, and minimums take place after the end of the accelerating phase. The trace of Ω^*_T also evolves with a low frequency $f^*_{\theta 3}/3 = f^*_{\theta 1}$ and the absolute maximums of vorticity accumulation near the cylinder are attained around the maximums of the torque (just after point b_2 in Fig. 12). The absolute minimums of vorticity accumulation coincide with the smallest torque maximum. See traces just past point a_3 in Fig. 12.

Although not shown explicitly in the figure, it is found that the (absolute) velocity ($\dot{\theta}$) in the interval a_1-a_3 is smaller than in the interval b_1-b_3. The opposite is true for the vorticity accumulation. The phenomena described here and in the following subsections are much better appreciated by looking at the actual time evolution given in the Supplemental Material [17].

4. Far wake

Before describing the distribution of vortices in the far wake, it must be observed that the vector sum of the azimuthal motion of the pendulum and the main horizontal flow results in local relative velocity oblique to the incoming flow. Consequently, the vortices are shed at an angle with respect to the horizontal line, and their centers are separated up to $1.5d$ from the horizontal line. This contrasts with the typical distance of $0.5d$ that is observed in the case of the fixed cylinder.

[2]Several ring widths in the range $0.1\text{d} < w < 0.2\text{d}$ were examined. All cases essentially give the same information; the case with the smoothest signal was chosen.

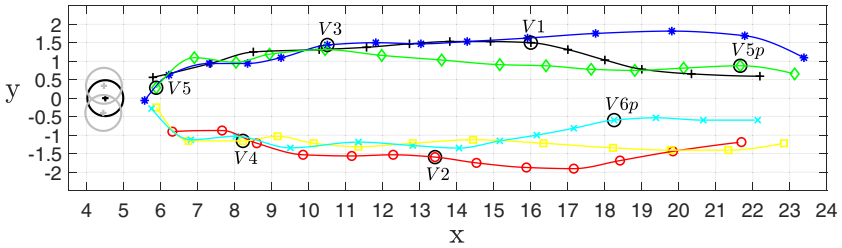

FIG. 13. Trajectories of the vortices. The black line represents the trajectory of the first negative vortex that corresponds to the positive displacement of θ in the large swing (see point a_1 of top panel in Fig. 11 and Supplemental Material [17]). The red line corresponds to the trajectory of the next vortex (first positive). The blue, yellow, green, and cyan lines represent, respectively, the third to sixth vortices. The empty black dots labeled with capital V's denote the position of the center of the vortices at $t^* = 980$ (see panel i Fig. 9). The cylinder's central and extreme positions are indicated by black and gray large circles on the left of the figure.

A superposition of the trajectories of the centers of the vortices in the wake of the moving cylinder is shown in Fig. 13 for a time interval slightly longer than one cycle of the cylinder motion. The center of a vortex is identified by the local maximum in the vorticity distribution. The vortex trajectory that is closer to the cylinder in Fig. 9(a) is the black line. This negative vorticity structure is labeled $V1$. The subsequent vortices are labeled $V2$, $V3$, etc., and their trajectories are coded according to the colors listed in the figure caption. Two pairs of trajectories (1st and 6th, black and cyan lines, and 4th and 5th, yellow and green lines) are approximately symmetric with respect to the horizontal line $\theta = 0$. To give a picture of the vortices' centers relative positions at a fixed time, we superpose empty black dots on the respective trajectories. Positions $V5p$ and $V6p$ indicate vortices were shed at the previous cycle.

As can be observed, the distance between $V1$, $V6p$, and $V5p$ is relatively small, and the vortices interact with each other as it is apparent from the subsequent vorticity fields shown in panels j to l in Fig. 9 where $V6p$ is sucked by vortices $V1$ and $V2$. This effect is consistent with the upward bend of the trajectory of $V6p$ (cyan trace).

The (negative) vortex that is generated at the oscillation with the largest torque contains maximum vorticity ($V5$), and it is followed by the oscillation of the longest duration (maximum wavelength) and maximum amplitude of cylinder displacement. The following vortex ($V1$) has a slightly smaller vorticity and merges with the previous and next vortices. This is suggested in Figs. 9(b) and 9(c) and is clearly seen in the movie of the Supplemental Material [17].

As a general property of the wake, it has been found that the extension of the vortices is related to the azimuthal displacement of the cylinder, while the intensity of the vorticity contained in a vortex is related to the torque, or equivalently, to the acceleration of the cylinder.

C. Pressure field and instantaneous streamlines

The dominant terms in the calculation of the forces and torque on the cylinder, Eqs. (14) and (15), respectively, are those containing the pressure. Thus, an alternative analysis of the cylinder's dynamics and the surrounding flow can be made in terms of the pressure field. Figure 14 shows the pressure field around the cylinder for the selected points indicated in the upper panel of the figure; note that the times coincide with those of Fig. 11.

The pressure field's most salient features include the pressure maximum, whose position on the cylinder's periphery is determined by the relative motion of the cylinder and the incoming flow and therefore has a cyclic displacement. The maximum pressure point corresponds to the stagnation point, which defines the boundary layer's symmetry referred to in the discussion Fig. 11. The pressure field downstream of the cylinder is closely related to vorticity generation in the boundary layer and the cyclical shedding of vortices. At position a_1, the pressure gradient generated by the

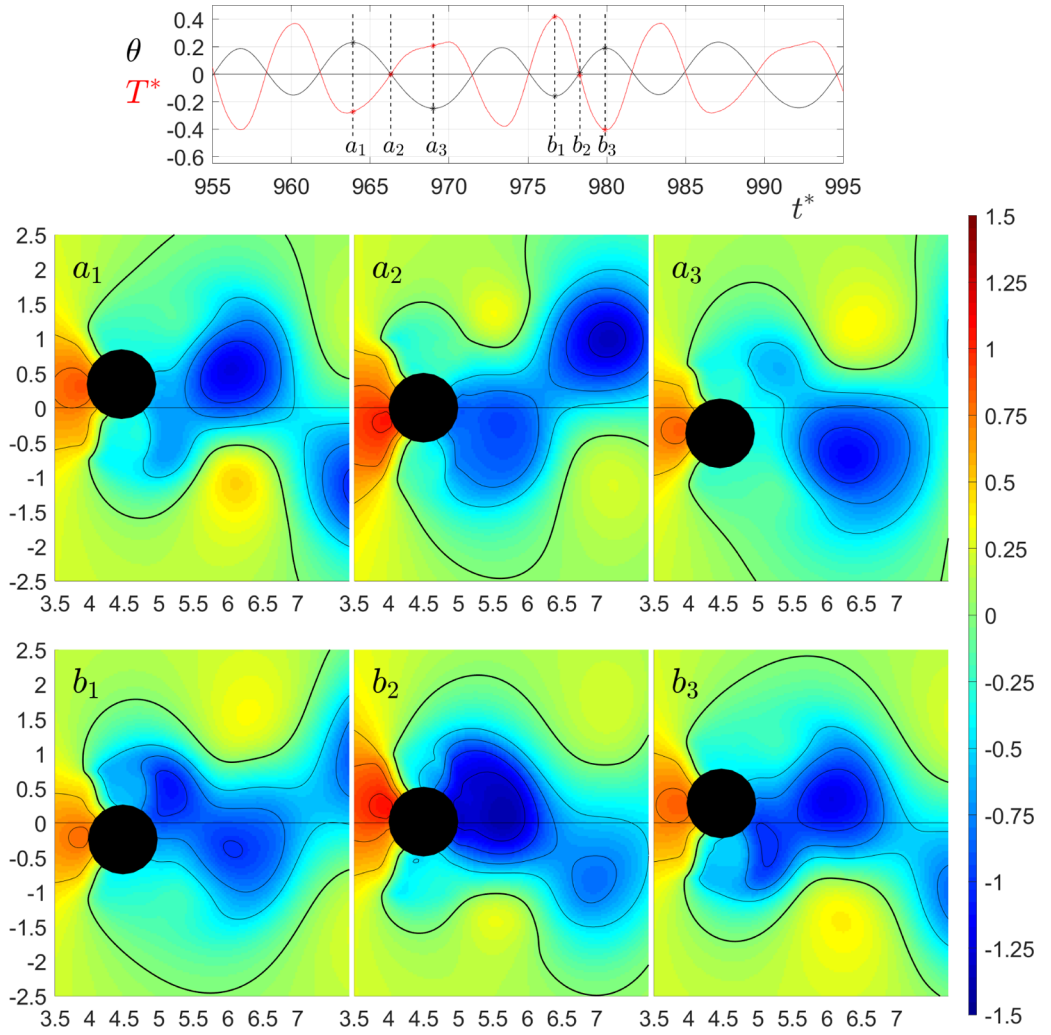

FIG. 14. Snapshots of pressure field. The cylinder's angular position and times where the fields were obtained are indicated in the upper panel.

diametrically opposed high and low-pressure points is almost horizontal, and the torque is at a local (negative) maximum. Zero torque coincides with no azimuthal displacement at position a_2 and a relatively small pressure difference across the diameter that includes the stagnation point results in a relatively small torque maximum as illustrated in a_3.

The pressure field corresponding to the time interval where the cylinder has a positive velocity ($\dot{\theta} > 0$) is shown in panels b_1 to b_3. At b_1, the cylinder is at its lowest position, and the torque reaches its overall maximum, the maximum pressure point is at the leading position of the cylinder because the azimuthal velocity is zero and the relative velocity runs along the x direction. In contrast, the low-pressure region is oblique, generating a large torque. The pressure field at b_2 is the reflection of that observed at a_2 because of the opposite direction of the cylinder's angular velocities. Also, the pressure intensity is larger in b_2.

The topology of the instantaneous streamlines has been used to describe the flow around the cylinder and to determine the evolution of vortex emission in fixed cylinders; see, for instance, Ref. [26]. This technique is also useful to analyze the present flow. Given that the flow is two-

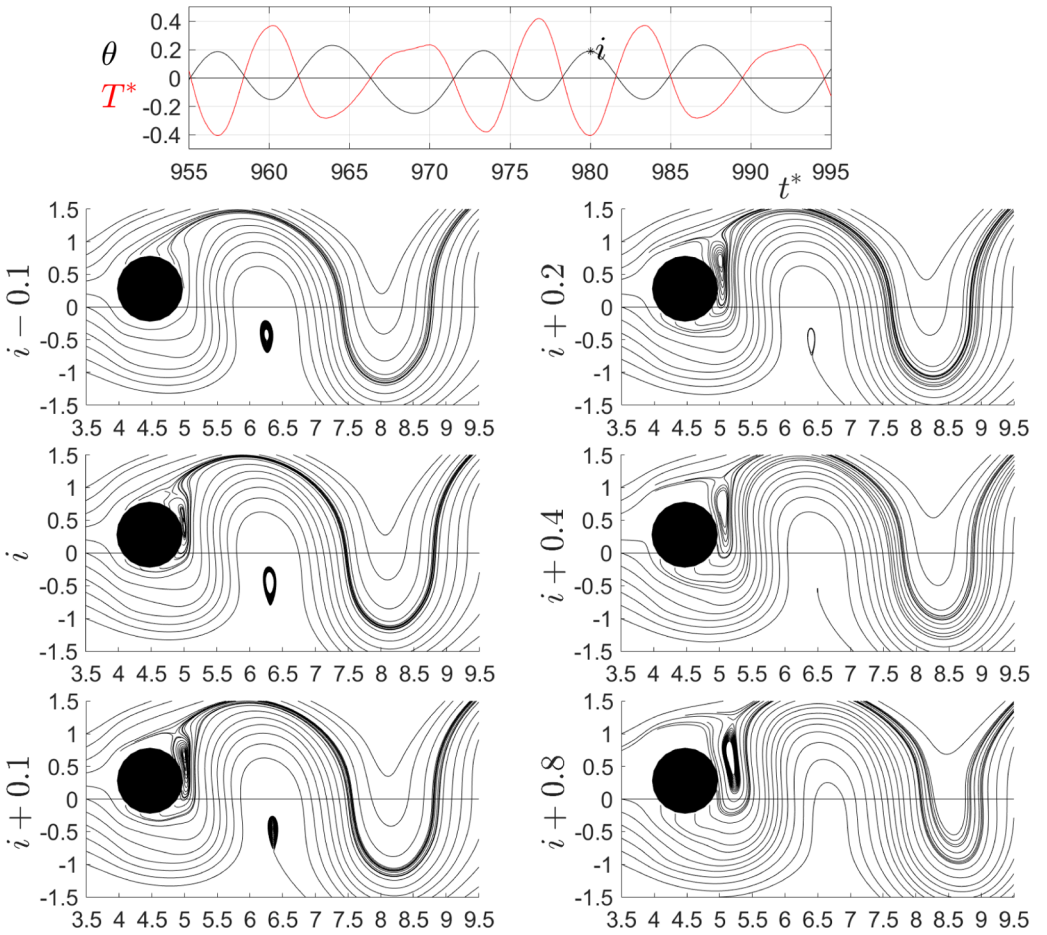

FIG. 15. Instantaneous streamlines near ($t^* = 980$) when the cylinder is at a maximum displacement. Point i in the upper panel. The decimal numbers in the labels are nondimensional time units.

dimensional, only two kinds of critical points, saddles and centers, also termed hyperbolic and elliptic points, respectively.[3] At the times of maximum (upper or lower) azimuthal displacements of the cylinder, it is observed that viscous saddles are formed alternatively at the (upper or lower) separation points. Shortly after, they are swept away to become inviscid saddles that determine the positions of the separatrices. Centers are generated simultaneously with saddles and are located closer to the horizontal symmetry line. It is found that the dynamics of the critical points are very fast, moving a distance of one cylinder diameter in less than a one-time unit. A specific example of these events is given in Fig. 15. In this figure, the instantaneous streamlines at times just before and closely after the cylinder is at its maximum displacement are shown (point i in the figure's upper panel). At $t^* = 980$, the saddle point that was just generated in the boundary layer is located at approximately ($x = 4.80$, $y = 0.92$). The corresponding center (elliptic point) is at ($x = 5.00$, $y = 0.40$). After 0.8 time units the two critical points have moved to ($x = 5.21$, $y = 1.18$) and ($x = 5.16$, $y = 0.62$), respectively. Note that at time $t^* = 980$, the center shed when the cylinder

[3]A critical point is where the slope of a streamline is indeterminate.

was at the previous lowermost position is located at ($x = 6.307$, $y = -0.453$) while its saddle point is out of the visualization area.

V. DISCUSSION AND CONCLUSIONS

The vibration of a cylinder exposed to a constant velocity flow in the absence of gravity has been analyzed using a numerical solution of the mass and momentum conservation equations coupled with the Euler equation. The immersed boundary method was implemented to account for the solid-fluid interactions.

The cylinder motion and the flow around it are two-way coupled. The cylinder vibrates driven by the forces generated by the fluid-solid interaction and, in turn, the incoming flow is perturbed by the presence and motion of the cylinder. The forces acting on the cylinder are asymmetric due to the alternating emission vortices resulting in an oscillatory motion.

The azimuthal position of the cylinder depends on the initial conditions, mostly in the transient region but also in the long-term dynamics. At long times, the cylinder exhibits a periodic motion with a cycle composed of three oscillations with slightly different amplitude and frequency. The harmonic content of the signal indicates that the dominant frequency corresponds to individual oscillations. Other relevant frequencies are related by factors of $1/3$. An interesting property of the results is that even after many cycles, the angular positions as functions of time are not identical in each cycle. The small variations between cycles have a definite structure in the phase space. This phenomenon has been labeled as quasiperiodic. Additionally, we observe that the torque on the cylinder is synchronous but out of phase with respect to the azimuthal position. The relative velocity periodically changes the location of the stagnation point, the boundary layer separation angles and, the vortices emission frequency. A related feature was observed in the forced oscillating cylinder. Blackburn and Henderson [7] found that the lift and drag coefficients in the quasiperiodic mode the dominant frequencies are commensurable.

In the nomenclature proposed by Williamson and Roshko [27], we found that single (S) vortices are emitted to form the von Karman-like wake, although in the present case, the wake is wider than that of the fixed cylinder. This feature is attributed to the fact that the relative velocity vector points at an angle with respect to the streamwise direction. In contrast to the fixed cylinder wake generated with a Reynolds number of 180, there is a strong interaction between the vortices in the wake, continuously altering its structure as the vortices are swept downstream.

It is interesting to describe the vorticity generation in the flow. Vorticity is produced at the rigid body-fluid boundary by the cross product of unit vector normal to the cylinder's surface, and the sum of the tangential pressure gradients and the acceleration of the rigid body [28]. In the flow under analysis, the two effects are at work. Tangential pressure gradients occur because of the flow modifications due to the obstacle's geometry; this effect is also present in a fixed cylinder. The vorticity generation due to this effect is similar to that occurring in the two cases. Also, given that the cylinder is in cyclic motion due to the rigid body-fluid interaction, a periodic acceleration and vorticity generation due to this effect are present. The amplitude of the oscillation along the circle of diameter D is small, and to simplify the discussion, we will consider that it occurs only in the $\pm y$ direction. The maximum absolute value of the acceleration takes place at the maxima of positive and negative displacements, and it is zero at position $y = 0$. The cross product of the acceleration and the unit vector perpendicular to the surface of the cylinder (and consequently the generation of vorticity due to acceleration) are maxima at the diametrically opposed points in the horizontal direction, i.e., the forward and rear points and zero at the upper- and lower-most points on the cylinder. The vorticity generated by acceleration is of opposite signs in the right and left sides of the cylinder, and it switches signs when the cylinder changes the direction of motion. The vorticity patch generated at the rear point is always of opposite sign to the vorticity in the region towards which it is moving. Once the vorticity is generated, it diffuses away from the boundary, interacts with the background vorticity, and is advected by the main flow.

Given that the cylinder is constrained to move around a circle, that the forces arising by the interaction have a large component in the streamwise direction, and that the torque is out of phase with the position, one would be tempted to interpret the motion as a gravitational pendulum, with the drag force playing the role of gravity. Moreover, the description of the pressure field around the cylinder suggests that the motion of the cylinder may be interpreted as that of a pendulum, where the restoring force is mostly generated by the pressure difference between the front and back halves of the cylinder. The buildup of positive pressure on the front of the cylinder is caused by the slowing down of the flow that changes kinetic energy into pressure. The negative pressure on the backside of the cylinder is produced by the shadowing of the flow by the presence of the cylinder. However, there are important differences that prevent us from considering a harmonic oscillator as a simplified model. The main differences are the following. On the one hand, the (time-dependent) transverse force also contributes to the torque, and thus to the restoring force depends on the cylinder's position. On the other hand, as shown in Fig. 5, the streamwise force is not constant as it is in a gravitational pendulum. Despite the previous comments, it is interesting to note some dynamical features of the cylinder's motion can be captured with a harmonic oscillator model with a time-dependent restoring force. This model is equivalent to a variable-length pendulum or a damped pendulum with a sliding mass. An appropriate choice of parameters reproduces the cycle composed of three quasiperiodic dynamics as reported by [29]. These models incorporate the fact that the system has two response times: The hydrodynamic time associated with the surrounding fluid's motion and the inertia time associated with the motion of the cylinder related to the solid to fluid densities. The development of simple models for the system reported is the subject of an ongoing research project.

As commented previously, the acceleration of gravity has not been included in the analysis. This represents the physical situation of vertical cylinders proposed in the literature for devices to extract marine energy where the acceleration of gravity is aligned with the axis of symmetry of the cylinder or for vertical axis wind turbines. Other configurations are possible where the force of gravity plays a role, like horizontal or inclined cylinders. Although beyond the scope of the present analysis, this effect may be incorporated in our model.

The present study has been restricted to fixed values of the parameters ($\mathrm{Re} = 180$, $m^* = 1.6$, $D/d = 3$). A natural question is: What are the corresponding features of the fluid-solid interactions for different parameters' values? As it is well known, three-dimensional effects appear in the wake of a cylinder for Reynolds numbers larger than about 190. Thus, this can be considered the upper limit for a two-dimensional analysis. Also, $m^* > 1.6$ would yield a smaller effect of the fluid's motion on the cylinder, but for $m^* < 1.6$, the interaction will be more intense and the analysis of the dynamics more challenging. Considering a larger radii ratio would make the computational effort considerably larger for equivalent precision. However, it would render the calculation more useful for applications related to vertical axis wind turbines.

ACKNOWLEDGMENTS

D.R.D. acknowledges with gratitude the Ph.D. grant from CONACYT (Mexico) and the economic support from Project No. 272063, "Fortalecimiento del Campo de Energía Eólica en el Programa de Doctorado en Ingeniería, Campo de Conocimiento en Energía con sede en el Instituto de Energías Renovables de la Universidad Nacional Autónoma de México," CONACYT-SENER (Mexico)-Sustentabilidad Energética, for supporting the development of this research work. We also thank the anonymous reviewers for useful comments on the original version of the article.

APPENDIX: NUMERICAL CONVERGENCE AND VALIDATION

To solve the mass and momentum conservation equations coupled with the Euler equation subject to the constraint that the cylinder moves with one azimuthal degree of freedom, we developed a code based on the finite volume method to discretize the conservation equations coupled with the immersed boundary method presented in Ref. [19].

TABLE I. Mesh sensitivity analysis. Fixed cylinder.

Mesh size	St	C_D
384×192	0.151	1.256
768×384	0.185	1.132
1,536×768	0.198	1.177
Experimental	0.19 [32]	1.29[33]
Shiels [30]		1.29
Henderson [31]		1.35

The mesh sensitivity analysis and the numerical code validation are made considering the flow around a fixed cylinder. To the best of our knowledge, no experimental or numerical results for the case under scrutiny have been published. We concentrate on the case Re= 180, which is the value considered in the present investigation, and also because, for these physical conditions, detailed experimental and numerical results are available. A two-dimensional analysis is expected to be valid for this case because three-dimensional effects in the flow for Re $<$ 190 are negligible [11]. Table I compares the wake oscillation frequency (Strouhal number St) and the drag coefficient (C_D) for different Cartesian 2D meshes with experimental values from the literature. Unfortunately, experimental uncertainty is not available. In these calculations, a domain with sides of $24d \times 12d$ is used. Table I also includes results from numerical calculations based on the viscous-vortex method [30] and on spectral element methods [31], that are reported in the literature.

The mesh refinement analysis indicates that the mesh 768×384 correctly predicts the Strouhal number and underestimates the drag coefficient obtained in experiments. Further refinement yields results closer to experimental observations. Still, as explained in the text, the transients are very long, most of the time requiring up to 4000 nondimensional time units which typically correspond to three months in wall clock time. For this reason, we concluded that the 768×384 mesh, which corresponds to 32×32 volumes in the d^2 area, is the best trade-off between total computational time and accuracy.

A domain size analysis was performed to find a proper computational domain that minimizes the boundaries' effect over the results on the flow around the cylinder. In Table II, the Strouhal number (St) and the RMS torque (T^*_{RMS}) are given for three different computational domains. It can be observed that with the $24d \times 12d$ and $30d \times 16d$, very similar results were obtained, but the computational time for the larger domain is three times that required for the $24d \times 12d$. Unfortunately, no experimental observations are available to compare with. Again, due to the computational cost, the domain of $24d \times 12d$ was selected to carry out all the simulations presented in this work. Additionally, temporal resolution tests were made, reducing the time step. Using $\delta t = 8, 4, 2,$ and 1×10^{-4} nondimensional units, the Strouhal number obtained was St = 0.172, 0.158, 0.129 and 0.131, respectively. This indicates that $\delta t = 2 \times 10^{-4}$ is the best choice for time step and CPU time.

TABLE II. Domain size analysis. Cylinder with azimuthal degree of freedom.

Dom. size	St	T^*_{RMS}
$16d \times 8d$	0.160	0.291
$24d \times 12d$	0.129	0.245
$30d \times 16d$	0.123	0.227
$32d \times 16d$	0.120	0.225

[1] R. D. Blevins, *Flow-induced Vibrations* (Van Nostrand Reinhold, New York, 1990).
[2] E. Naudascher and D. Rockwell, *Flow-induced Vibrations: An Engineering Guide* (Balkema, Rotterdam, Netherlands, 1994.
[3] B. M. Sumer and J. Fredsoe, *Hydrodynamics Around Cylindrical Structures* (World Scientific, Singapore, 1997).
[4] C. H. K. Williamson and R. Govardhan, Vortex-induced vibrations, Annu. Rev. Fluid Mech. B/Fluids **36**, 413 (2004).
[5] A. Kahlak and C. H. K. Williamson, Dynamics of a hydroelastic cylinder with very low mass and damping, J. Fluids Struct. **10**, 455 (1996).
[6] A. Kahlak and C. H. K. Williamson, Motions, forces and mode transitions in vortex-induced vibrations at low mass damping, J. Fluids Struct. **13**, 813 (1999).
[7] H. M. Blackburn and R. D. Henderson, A study of two-dimensional flow past an oscillating cylinder, J. Fluid Mech. **385**, 255 (1999).
[8] J. R. Meneghini and B. W. Bearman, Numerical simulation of high amplitude oscillatory flow about a circular cylinder, J. Fluids Struct. **9**, 435 (1995).
[9] H. G. Sung, H. Baek, S. Hong, and J. S. Choi, Numerical study of vortex-induced vibration of pivoted cylinders, Ocean Eng. **93**, 98 (2015).
[10] H. Arionfard and Y. Nishi, Experimental investigation of a drag assisted vortex-induced vibration energy converter, J. Fluids Struct. **68**, 48 (2017).
[11] C. H. K. Williamson, Vortex dynamics in the cylinder wake, Annu. Rev. Fluid Mech. **28**, 477 (1996).
[12] H. Arionfard and Y. Nishi, Added mass moment of inertia of a rotationally oscillating surface-piercing circular cylinder in still water, in *Proceedings of the 9th JSME-KSME Thermal and Fluids Engineering Conference* (2017), paper TFEC9-1268.
[13] S. Kheirkhah, S. Yarusevych, and S. Narasimhan, Orbiting response in vortex-induced vibrations of a two-degree-of-freedom pivoted circular cylinder, J. Fluids Struct. **28**, 343 (2012).
[14] E. Marble, Ch. Morton, and S. Yarusevych, Vortex dynamics in the wake of a pivoted cylinder undergoing vortex-induced vibrations with elliptic trajectories, Exp. Fluids **59**, 78 (2018).
[15] C. Evangelinos and G. Karniadakis, Dynamics and flow structures in the turbulent wake of rigid and flexible cylinders subject to vortex-induced vibrations, J. Fluid Mech. **400**, 91 (1999).
[16] F. Oviedo-Tolentino, F. Pérez-Gutiérrez, R. Romero-Méndez, and A. Hernández-Guerrero, Vortex-induced vibration of a bottom fixed flexible circular beam, Ocean. Eng. **88**, 463 (2014).
[17] See Supplemental Material at http://link.aps.org/supplemental/10.1103/PhysRevFluids.6.064701 for movies.
[18] C. H. K. Williamson, The natural and forced formation of spot-like "vortex dislocations" in the transition of a wake, J. Fluid Mech. **243**, 393 (1992).
[19] G. Tryggvason, R. Scardovelli, and S. Zaleski, *Direct Numerical Simulations of Gas-Liquid Multiphase Flows* (Cambridge University Press, Cambridge, 2011).
[20] S. Piedra, J. Roman, A. Figueroa, and S. Cuevas, Flow produced by a free-moving floating magnet driven electromagnetically, Phys. Rev. Fluids **3**, 043702 (2018).
[21] C. Peskin, Numerical analysis of blood flow in the heart, J. Comput. Phys. **25**, 220 (1977).
[22] R. Glowinski, T. W. Pan, T. I. Hesla, D. D. Joseph, and J. Périaux, A fictitious domain approach to the direct numerical simulation of incompressible viscous flow past moving rigid bodies: Application to particulate, Flow. J. Comput. Phys. **169**, 363 (2001).
[23] L. H. Juárez and R. Glowinski, Numerical simulation of the motion of pendula in an incompressible viscous fluid by lagrange multiplier/fictitious domain methods, in *Proceedings of the 14th International Conference on Domain Decomposition Methods* (Cocoyoc, Morelos, Mexico, 2002), pp. 185–192.
[24] S. Piedra, E. Ramos, and J. R. Herrera, Dynamics of two-dimensional bubbles, Phys. Rev. E **91**, 063013 (2015).
[25] C. H. K. Williamson, Defining a universal and continuous Strouhal-Reynolds number relationship for the laminar vortex shedding of a circular cylinder, Phys. Fluids **31**, 2742 (1988).
[26] A. E. Perry, M. S. Chong, and T. T. Lim, The vortex shedding process behind two-dimensional bluff bodies, J. Fluid Mech. **116**, 77 (1982).

[27] C. H. K. Williamson, and A. Roshko, Vortex formation in the wake of an oscillating cylinder, J. Fluid Struct. **2**, 355 (1988).
[28] B. R. Morton, The generation and decay of vorticity, Geophys. Astrophys. Fluid Mech. **28**, 277 (1984).
[29] A. Klokov, Global analysis of dynamics of the pendulum systems, new bifurcation groups and rare attractors, Ph.D. thesis, Riga Technical University, 2013.
[30] D. Shiels, Simulation of controlled bluff body flow with a viscous vortex method, Ph.D. thesis, California Institute of Technology, 1998.
[31] R. D. Henderson, Details of the drag curve near the onset of vortex shedding, Phys. Fluids **7**, 2102 (1995).
[32] C. H. K. Williamson and G. L. Brown, A series in $1/\sqrt{\mathrm{Re}}$ to represent the Strouhal-Reynolds number relationship of the cylinder wake, J. Fluid Struct. **12**, 1073 (1998).
[33] D. J. Tritton, Experiments on the flow past a circular cylinder at low Reynolds numbers, J. Fluid Mech. **6**, 547 (1959).